**ARTICLE**

# Mitochondrial 4-HNE derived from MAO-A promotes mitoCa²⁺ overload in chronic postischemic cardiac remodeling

Yohan Santin[1] · Loubina Fazal[1] · Yannis Sainte-Marie[1] · Pierre Sicard[1,2] · Damien Maggiorani[1] · Florence Tortosa[1] · Yasemin Yücel Yücel[3] · Lise Teyssedre[4] · Jacques Rouquette[4] · Marlene Marcellin[5] · Cécile Vindis[1] · Jean C. Shih[6] · Olivier Lairez[1] · Odile Burlet-Schiltz[5] · Angelo Parini[1] · Frank Lezoualc'h[1] · Jeanne Mialet-Perez [1]

## Abstract

Chronic remodeling postmyocardial infarction consists in various maladaptive changes including interstitial fibrosis, cardiomyocyte death and mitochondrial dysfunction that lead to heart failure (HF). Reactive aldehydes such as 4-hydroxynonenal (4-HNE) are critical mediators of mitochondrial dysfunction but the sources of mitochondrial 4-HNE in cardiac diseases together with its mechanisms of action remain poorly understood. Here, we evaluated whether the mitochondrial enzyme monoamine oxidase-A (MAO-A), which generates $H_2O_2$ as a by-product of catecholamine metabolism, is a source of deleterious 4-HNE in HF. We found that MAO-A activation increased mitochondrial ROS and promoted local 4-HNE production inside the mitochondria through cardiolipin peroxidation in primary cardiomyocytes. Deleterious effects of MAO-A/4-HNE on cardiac dysfunction were prevented by activation of mitochondrial aldehyde dehydrogenase 2 (ALDH2), the main enzyme for 4-HNE metabolism. Mechanistically, MAO-A-derived 4-HNE bound to newly identified targets VDAC and MCU to promote ER-mitochondria contact sites and MCU higher-order complex formation. The resulting mitochondrial $Ca^{2+}$ accumulation participated in mitochondrial respiratory dysfunction and loss of membrane potential, as shown with the protective effects of the MCU inhibitor, RU360. Most interestingly, these findings were recapitulated in a chronic model of ischemic remodeling where pharmacological or genetic inhibition of MAO-A protected the mice from 4-HNE accumulation, MCU oligomer formation and $Ca^{2+}$ overload, thus mitigating ventricular dysfunction. To our knowledge, these are the first evidences linking MAO-A activation to mitoCa²⁺ mishandling through local 4-HNE production, contributing to energetic failure and postischemic remodeling.

---

Edited by L. Scorrano

✉ Angelo Parini
  angelo.parini@inserm.fr

✉ Jeanne Mialet-Perez
  jeanne.perez@inserm.fr

1   Institute of Metabolic and Cardiovascular Diseases (I2MC), INSERM, Université de Toulouse, Toulouse, France

2   INSERM, CNRS, Université de Montpellier, PHYMEDEXP, Montpellier, France

3   Department of Biochemistry, School of Pharmacy, Altinbas University, Istanbul, Turkey

4   ITAV, CNRS, Université de Toulouse, Toulouse, France

5   Institut de Pharmacologie et de Biologie Structurale, CNRS, Université de Toulouse, UPS, Toulouse, France

6   University of Southern California, Los Angeles, CA, USA

## Introduction

Postmyocardial infarction (MI) remodeling is a detrimental mechanism leading to heart failure (HF) and poor patient outcome. Although it is known that chronic remodeling consists in various maladaptive changes such as cardiomyocyte death, interstitial fibrosis, inflammation, and contractile dysfunction, there is still a strong need to better understand underlying pathological processes in order to develop novel therapeutic strategies. Mitochondrial dysfunction has emerged as a key player in post-MI ventricular failure and new advances put forward that mitochondria-targeted therapeutics may lead to improved energy production in the heart and better contractile function [1]. Mitochondria control key processes of cardiac remodeling such as ATP production, lipid metabolism, cell survival/death, and calcium ($Ca^{2+}$) buffering [2]. Uptake of cytosolic $Ca^{2+}$ into mitochondrial matrix regulates important enzymes of the Krebs cycle and electron transport chain and is necessary for matching energy supply to

the demand [3]. Hence, deregulation of mitochondrial $Ca^{2+}$ (mito$Ca^{2+}$) levels contribute to energetic failure in rodent models of HF, implying that its concentration needs to be fine-tuned thanks to the activity of the mito$Ca^{2+}$ uniporter (MCU) and the $Na^+/Ca^{2+}$ exchanger [4, 5]. In the particular situation of chronic ischemia, it is still unclear how mito$Ca^{2+}$ is regulated and contributes to cardiac remodeling, especially when it is accompanied by another stressor, oxidative stress [3].

Mitochondria are the main source of cellular reactive oxygen species (ROS) and, when exceeding antioxidant capacities, ROS can lead to the oxidation of fatty acids in a process termed lipid peroxidation [6]. Mounting evidence has linked lipid peroxidation with various human pathological states, such as neurodegenerative diseases, cancer, diabetes, and HF. 4-hydroxy-trans-2-nonenal (4-HNE) is the most abundant lipid peroxidation product and forms adducts with proteins, thereby affecting their biological function to impair cellular homeostasis [7]. Interestingly, 4-HNE levels are elevated in plasma of HF patients and inversely correlate with cardiac function [8]. Furthermore, enhancing the degradation of mitochondrial 4-HNE is beneficial in rodent models of acute and chronic heart diseases [9, 10]. At present, there is a strong need to identify the source of mitochondrial 4-HNE in pathological states and to understand the underlying mechanisms of its toxicity on mitochondrial function.

The monoamine oxidase-A (MAO-A) is an enzyme located at the outer mitochondrial membrane which represents the main degradative pathway for catecholamines and serotonin. MAO-A generates $H_2O_2$ as a by-product of substrate metabolism and has been recognized as a significant source of mitochondrial ROS in the heart [11, 12]. During post-MI remodeling, the sustained sympathetic drive and chronic elevation of circulating catecholamines could fuel MAO-A activity and ROS generation leading to 4-HNE production. To date, this putative role of MAO-A in post-MI remodeling has never been investigated.

In the present study, we found that MAO-A was responsible for an intramitochondrial generation of 4-HNE that, in turn, bound to voltage-dependent anion channel (VDAC) and MCU proteins, leading to mito$Ca^{2+}$ overload and impaired mitochondrial function. In ischemic failing human heart samples, there was a concomitant increase in MAO-A levels and 4-HNE-bound proteins and selective inactivation of MAO-A in mice with chronic MI prevented cardiac remodeling, 4-HNE accumulation, and mito$Ca^{2+}$ overload.

## Methods

### Human heart tissues

All studies are conformed to the Declaration of Helsinki and institutional ethical regulations. Informed consent was obtained from all subjects. Human failing hearts samples were a kind gift from Dr J.L. Samuel (Lariboisière Hospital, France). Explanted failing hearts were obtained from patients undergoing cardiac transplantation for end-stage cardiac HF secondary to ischemic cardiomyopathy. All patients had New York Heart Association (NYHA) Class IV HF, with a mean pretransplant left ventricular EF of $22 \pm 4\%$. None had received chronic intravenous inotropic support over at least 7 days immediately prior to transplantation. HF therapy consisted of angiotensin converting enzyme inhibitors and diuretics in all patients. Nonfailing hearts were obtained from prospective multiorgan donors who had died from head trauma or intracranial bleeds; these hearts were unsuitable for transplantation for technical reasons. All tissues were stored at $-80\,°C$ until further analyses.

### Animal models

All animal procedures were performed in accordance with International Guidelines on Animal Experimentation and with a French Ministry of Agriculture license. Moreover, this investigation conformed to the guide for Care and Use of Laboratory Animals published by the Directive 2010/63/ EU of the European Parliament. All mice were housed in temperature-controlled cages with a 12-h light–dark cycle and given free access to water and food. *MAO-A cKO mice*: maoa gene on Chromosome X was floxed with two LoxP sites around Ex12 in the laboratory of JCS (University of Southern California, CA, USA) [13]. The Myh6-Cre mice expressing Cre recombinase in cardiomyocytes were purchased from Janvier labs. The males with cardiomyocyte-specific deletion of Maoa (Maoa$^{fl/Y} \times$ Cre$^+$, referred as MAO-A cKO) and their control littermates (Maoa$^{WT/Y} \times$ Cre$^+$, referred as WT) on the C57Bl6J background were obtained by crossing Maoa$^{WT/Y} \times$ Cre$^+$ males with Maoa$^{WT/fl}$ females. *MAO-A Tg mice:* MAO-A transgenic mice (MAO-A Tg) on the C57Bl6J background were maintained by breeding of MAO-A Tg males (Myh6-maoa) with C57BL6/ J females [12]. MAO-A Tg males and their WT littermates were used for the experiments. *AAV9 model:* AAV9-cTnT-GFP and AAV9-cTnT-ALDH2 were purchased from Penn Vector Core (PA, USA). AAV9-cTnT-ALDH2 was made from the cDNA of mouse aldehyde dehydrogenase 2 (ALDH2) cloned into pCMV6-Entry vector (OriGene, Rockville, USA). The AAV9 vectors were injected by i.v.in the jugular vein of 3-week-old mice under anesthesia at a dose of $3 \times 10^{11}$ vg/mouse. Mice were kept for 4 months to assess cardiac remodeling.

### Myocardial ischemia

Mice were anaesthetized by 2% isoflurane inhalation. After orotracheal intubation, mice were mechanically

ventilated (minivent type 845, harvard apparatus) with 100% oxygen. Analgesia was provided by buprenorphine injection (0.02 mg/kg s.c.) and local lidocaine injection (50 μL of 10 mg/mL solution). Electrocardiogram (ADinstrument) was used to monitor the mice during the procedure. A left thoracotomy was performed at the 4th intercostal space to expose the heart. After opening of the pericardium using an 8-0 pvdf suture, the left anterior descending (LAD) coronary artery was tied 1 mm below the tip of the left auricle. Ischemia was verified by the sudden regional paleness of the myocardium and ST elevation. The chest cavity was closed by bringing the ribs together with 6-0 suture while pressure was applied at the level of the xyphoïd process. Muscle and skin layers were closed and the anesthesia was stopped. Mice were extubated at first sign of waking up and allowed to recover in a heating box. Only LAD ligation was omitted in the SHAM procedure. *Moclobemide treatment*: moclobemide was given 15 min after coronary artery ligation by IP injection at a dose of 20 mg/kg. In the following day, moclobemide was given in the drinking water at a concentration of 20/mg/kg/day and kept during the 4 remaining weeks. The number of animals required for the study has been evaluated from the first validation experiment performed on a small cohort of mice ($n = 12$). Power analysis was conducted to estimate the appropriate sample size by setting the probability of a Type I error (α) at 0.05, power at 0.95, and effect size at 1.5.

## Echocardiography

Mice were anesthetized with 2% isoflurane and examined with noninvasive echocardiography (Vivid 7 ultrasound, GE; vevo2100 Visual Sonics). Cardiac ventricular dimensions were measured in a blinded fashion on M-MODE/2D images for the number of animals indicated.

## Whole heart imaging

Heart optical clearing was performed as follow. Formalin-fixed hearts were dehydrated with three successive immersions in 100% methanol solutions. Samples were transferred into methanol/BABB solution (one part benzyl alcohol, two parts benzyl benzoate, and three parts of methanol) then in BABB solution (one part benzyl alcohol and two parts benzyl benzoate), and incubated for 2 days. Cleared hearts were imaged using Light-Sheet Fluorescence Microscopy (LSFM) as described in Abadie et al. [14]. Images were processed with the open-source image-processing Fiji. 3D volume rendering, segmentation and measurements were performed with Amira® software (FEI Visualization Sciences Group, Hillsborough, OR, USA).

## Primary cultures of cardiomyocytes

### Neonatal rat ventricular myocytes (NRVM) isolation

Neonatal rats of 1–2 days old were euthanized by decapitation. The heart was excised and the atria were removed. Primary culture of NRVMs was subsequently performed as previously described [15]. NRVMs were transduced with an adenovirus expressing rat MAO-A under the control of the CMV promoter to drive expression of MAO-A. After 24 h, the medium was replaced with Ham-F12 medium supplemented with 3% dialyzed FBS, and pharmacological treatments were performed.

### Adult mice cardiomyocytes (AMCMs)

The heart was quickly excised, and the aorta was cannulated for retrograde perfusion in a Langendorff apparatus at a constant flow rate of 3 mL/min at 37 °C as previously described [16]. Freshly isolated cardiomyocytes were plated on laminin-coated culture dishes in M199 complete medium (M199 medium with added 100 IU/mL penicillin, 2 mmol/L L-carnitine, 5 mmol/L creatine, and 5 mmol/L taurine) at 37 °C in a humidified atmosphere with 5% CO$_2$. The culture protocol yielded an average of 80% rod-shaped myocytes at a plating density of 50 cells/mm$^2$ that were viable at pH 7.2 for 48 h.

## Mitochondria isolation

Hearts were excised, washed in phosphate-buffered saline (PBS), and crushed using a tissue grinder in mitochondrial isolation buffer (0.3 M sucrose, 5 mM TES, and 200 μM EGTA) supplemented with Proteinase bacterial (Sigma-Aldrich). Mitochondrial isolation buffer supplemented with BSA was then added to the homogenates before centrifugation at 500 g for 10 min at 4 °C. Supernatant was collected and centrifuged at 3000 g for 10 min at 4 °C and pellet corresponding to mitochondria was either immediately used (for mitoH$_2$O$_2$, mitoNAD$^+$/NADH, mitoCa$^{2+}$ measurements) or kept at −80 °C (for western blots, LC-MS/MS for cardiolipin (CL) and HODEs).

## Immunofluorescence and histological studies

Heart tissues were embedded in optimal cutting temperature compound (OCT) (Sigma-Aldrich) under ice-cold 2-methylbutane. For immunofluorescence studies, frozen sections (5 μm) were fixed in 4% paraformaldehyde, followed by permeabilization and blocking in PBS with 0.02% FBS, 1% bovine serum albumin, and 0.3% Triton X-100 at RT. Sections were immunostained overnight with the following antibodies: anti-4-HNE (Abcam 46545), anti-Vinculin (Sigma-Aldrich V9131) followed by secondary

Alexafluor antibodies (Molecular Probes). Nuclei were visualized with DAPI. Images were acquired by confocal Microscope Zeiss LSM 780 and ZEN image analysis software (Zeiss) or digitized with a Hamamatsu NanoZoomer and fluorescence intensity was quantified by ImageJ software. Average cardiomyocyte diameter and the number of cardiomyocytes per total myocardial area were measured manually after vinculin staining (500–600 cells counted per heart) on six different regions of the peri-infarct zone. For fibrosis, hearts were transversely sectioned at 1-µm thickness, fixed with 4% paraformaldehyde and stained with Masson's Trichrome. Fibrosis was measured as positively stained area with Masson's Trichrome and expressed as percent of total area, using ImageJ software (RSB). For NRVMs, cells stained with MitoTracker™ Red (Thermo Fischer Scientific M22425) were fixed with 4% PFA and incubated in TBS-0.2% triton O/N at 4 °C with 4-HNE antibody. After secondary antibody (anti-rabbit IgG Alexafluor 488, Invitrogen), slides were observed under confocal microscopy (LSM 780, Carl Zeiss).

## Western blot

Total extracts of ventricle or NRVMs were lysed in RIPA buffer (50 mM Tris pH 7.2, 500 mM NaCl, 1% Triton X-100, 1 mM EDTA, 100 mM sodium fluoride, 5 mM sodium metavanadate, and 10 mM sodium pyrophosphate) and equal protein amounts were subjected to SDS-PAGE. After electrophoresis, proteins were transferred to PVDF membranes and immunoblotted with the following antibodies: anti-4-HNE (Abcam 46545), anti-MAO-A (Abcam 126751), anti-ALDH2 (Abcam 108306), anti-GAPDH (CST5174), anti-Vinculin (Sigma V9131), anti-COX-IV (CST4844), anti-CBARA1/MICU1 (CST12524), anti-EFHA1/MICU2 (Abcam 101465), anti-MCU (CST14997), and anti-VDAC1 (CST4866). Proteins were detected by chemiluminescence with a Bio-Rad ChemiDoc. Relative densities were quantified using the ImageLab 5.2.1 software (Bio-Rad). All data were normalized by internal controls.

## Immunoprecipitation

NRVMs, AMCMs, or heart tissues were lysed in buffer containing 20 mmol/L Tris, pH 7.5, 150 mmol/L NaCl, 1 mmol/L EDTA, 1% Triton X-100, protease and phosphatase cocktail inhibitors (Roche). Proteins were put in agitation O/N at 4 °C with 5–10 µg of appropriated antibodies. Purification steps were performed with protein A/G agarose according to the manufacturer's instructions (SantaCruz Biotechnologies). For improved western blotting detection to avoid heavy and light chains signals, blots were incubated 2 h at RT with a Protein G-HRP (dilution 1:5000,

Biorad), prepared in blocking buffer. After washing with TBST, blots were developed with ECL Plus (Amersham Biosciences).

## ALDH2 activity, GSH measurements, and ATP content

ALDH2 activity was determined in ventricular homogenates or NRVMs using the ALDH2 assay kit (Abcam). GSH content was evaluated in ventricle samples using the "Total Glutathione detection kit" from Assay Designs (Enzo life sciences). Intracellular ATP content was determined by measuring the conversion of D-luciferin to oxyluciferin using the ATP bioluminescence assay kit II according to the manufacturer's instructions (Roche).

## Mitochondrial H$_2$O$_2$

Cells were incubated with mitoPY1 probe (Mitochondria Peroxy Yellow-1, Sigma) at a final concentration of 10 µM at 37 °C for 60 min. Mitochondrial specificity was confirmed by co-staining with MITO-ID Red (Enzo life sciences). Representative pictures were taken with a confocal microscope (LSM 780, Carl Zeiss). Mitochondrial H$_2$O$_2$ production in mouse hearts was measured using fluorescent probe Amplex Red (10 µmol/L) in the presence of 0.6 U/ml horseradish peroxidase (excitation and emission wavelengths set to 530 and 590 nm, respectively) on isolated mitochondria.

## Mitochondrial membrane potential (ΔΨm)

TMRE (Tetramethylrhodamine, ethyl ester) probe was added to each well at a final concentration of 500 nm at 37 °C for 30 min. Then, medium was replaced by HBSS and the fluorescence was recorded in the presence or not of FCCP at Ex/Em = 549/575 nm, using a fluorimeter TECAN infinite pro F200.

## Mitochondrial respiration

Oxygen consumption rate (OCR) was measured in AMCMs with a Seahorse XFe24 Analyzer (Agilent). Cells were plated in laminin-coated Seahorse 24-well assay plates (2500 cells per well) in M199 complete medium. After 2 h of cell attachment, cell medium was replaced with XF base medium supplemented with 10 mM glucose, 4 mM L-glutamine and 1 mM sodium pyruvate (pH 7.4), and maintained at 37 °C for 1 h. The wells of a hydrated sensor cartridge were then loaded with 1 µM oligomycin (port A), 1 µM FCCP (port B), and 1 µM antimycin A + 1 µM rotenone (port C). Data were analyzed with Seahorse Wave software. Maximal respiratory capacity was calculated by

Mitochondrial 4-HNE derived from MAO-A promotes mitoCa$^{2+}$ overload in chronic...

1911

subtracting the nonmitochondrial OCR (minimum rate measurement after antimycin A/rotenone injection) from the OCR after FCCP injection. Spare respiratory capacity was calculated by subtracting the baseline OCR from the OCR after FCCP injection.

## Measurement of mitochondrial Ca$^{2+}$ uptake

Intact cardiomyocytes or freshly isolated mitochondria were suspended in Tyrode buffer and incubated with 10 μmol/L Rhod-2-acetoxymethyl ester (Rhod-2-AM; Life Technologies, France) for 30 min at 4 °C, and then for 30 min at 37 °C [16]. With this cold loading/warm incubation procedure, Rhod-2-AM localized to mitochondria. Typically, successive 1 ml aliquots of cells/mitochondria suspension were loaded and experimented on for the same amount of time. Fluorescence ($\lambda$ excitation: 540 nm, $\lambda$ emission: 605 nm) was acquired from cells/mitochondria treated or not with Rhod-2-AM on a Varioskan Flash Multimode Microplate Reader for 270 s. In each experiment, 20 μmol/L CaCl$_2$ was added. Experiments were performed at least with 5–6 mice/group.

## Duolink proximity ligation in situ assay

Briefly adult mouse cardiomyocytes were fixed with 4% paraformaldehyde and permeabilized with 0.1% Triton X-100. Subsequent blocking, antibody hybridizations, proximity ligations, and detections were performed according to recommendations from manufacturers (OLINK Bioscience, Sigma-Aldrich, France). The cells were incubated with the primary antibodies overnight at 4 °C and then washed three times with TBS-0.05% Tween 20. Briefly, after incubation with primary antibodies, we applied combinations of corresponding in situ proximity ligation assay (PLA) probes for 1 h at 37 °C. The cells were washed with TBS-0.05% Tween 20, incubated for 30 min with ligase, and finally washed with TBS-0.05% Tween 20. Then cells were incubated with polymerase for 100 min. Fluorescence was analyzed with a laser confocal Zeiss LSM 780 microscope. Quantification of signals was performed with BlobFinder software (Center for Image Analysis, Uppsala University) and expressed as interactions per cell relative to the nontreated group. Experiments were performed at least four times, with a minimum of 6–8 fields taken per condition.

## Size-exclusion chromatography

Cells were washed in PBS and lysed in IP buffer (20 mmol/L Tris, pH 7.5, 150 mmol/L NaCl, 1 mmol/L EDTA, 1% Triton X-100, protease and phosphatase inhibitors cocktail (Roche)). Using an AKTA purifier 10 (GE Life Science),

lysates were injected (200 μL per injection) onto a Superose 6 10/300GL column (GE Life Sciences) equilibrated with IP Buffer (pH 7.5). The flow rate was 0.2 mL min$^{-1}$ and 40× 400 μL fractions were collected using a low protein binding 96-deep-well plate Eppendorf (Hamburg, Germany) and tested on western blots. The system was previously calibrated with high molecular weight markers (GE Life Science). The annotated molecular weights were estimated from the elution profiles of standard markers injected onto the SEC column.

## Statistical analysis

Statistical analysis was carried out using Student's $t$ test or two-way ANOVA with the Tukey post hoc test, when appropriate. Lung edema was analyzed statistically using chi square test. The results are shown as the mean ± SEM. Values of $p < 0.05$ were considered to be significant.

# Results

## MAO-A activation promotes intramitochondrial 4-HNE formation through CL peroxidation

We first sought to determine whether MAO-A influenced mitochondrial 4-HNE. Application of tyramine (Tyr), a MAO substrate, led to 4-HNE mitochondrial accumulation in AMCMs, as revealed by co-staining of 4-HNE with the mitochondrial marker Mito-ID (Fig. 1a and Supplementary Fig. 1A). In transgenic mice with cardiac overexpression of MAO-A, a model of oxidative stress and HF (MAO-A Tg) [12], isolated mitochondria showed accumulation of 4-HNE-bound proteins compared with WT mice (Fig. 1b). 4-HNE can be formed upon ROS-dependent peroxidation of lipids, in particular CL the signature phospholipids of mitochondrial inner membrane, via the synthesis of hydroxyoctadecadienoic acids (HODEs) [17]. We thus investigated whether MAO-A favored intramitochondrial 4-HNE accumulation through ROS-dependent CL peroxidation. In AMCMs, application of Tyr for 30 min increased mitochondrial H$_2$O$_2$, as shown by overlapped staining of the H$_2$O$_2$-sensitive probe MitoPY1 with Mito-ID red (Fig. 1c and Supplementary Fig. 1B). Consistently, mitochondria of MAO-A Tg hearts also displayed elevated levels of H$_2$O$_2$ compared with WT (Fig. 1d). In NRVMs transduced with MAO-A adenovirus, Tyr-induced mitoH$_2$O$_2$ accumulation preceded the accumulation of 4-HNE (at 1 h and later) (Supplementary Fig. 1C–E). We next performed LC–MS/MS to analyze mitochondrial content in CL and HODEs. The major species tetralinoleoylcardiolipin (L$_4$CL or 72:8) was significantly decreased in MAO-A Tg mitochondria compared with WT (Fig. 1e and Supplementary Fig. 1F). This is particularly interesting since L$_4$CL is the most abundant CL in mammalian tissues, and is the only form
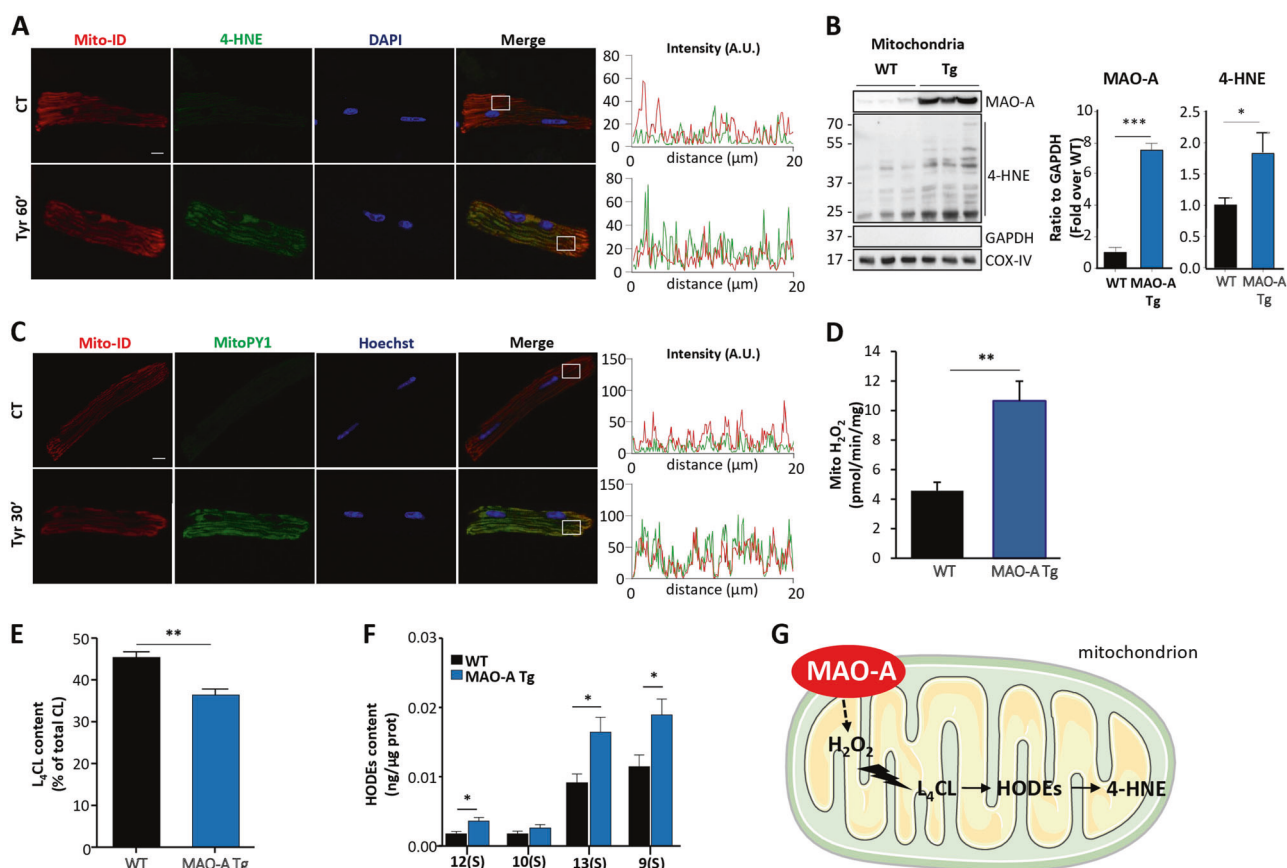
**Fig. 1 MAO-A activation leads to intramitochondrial 4-HNE production through $H_2O_2$-mediated $L_4CL$ peroxidation. a** Representative confocal images of 4-HNE staining (green) on AMCMs isolated from WT mice loaded with Mito-ID red and counterstained with DAPI (blue). Cells were treated with 50 μM Tyr for 1 h. Scale Bar = 10 μm. $n = 5$. **b** Immunoblots of MAO-A expression and 4-HNE protein adducts and quantifications in isolated mitochondria of WT and MAO-A Tg hearts at 12 weeks ($n = 6$ per group). **c** Representative confocal images of MitoPY1 (green), Mito-ID (red), and Hoechst 33258 staining on AMCMs isolated from WT mice treated with 50 μM Tyr for 30 min. Scale Bar = 10 μm. $n = 5$. **d** Amplex red measurements in isolated mitochondria of WT and MAO-A Tg hearts ($n = 5$) at 12 weeks. Quantifications by LC–MS/MS in isolated mitochondria of WT ($n = 6$) and MAO-A Tg ($n = 4$) hearts at 12 weeks showing (**e**) $L_4CL$ content as percent of total cardiolipin and (**f**) each type of HODEs species as ng/μg prot. **g** Proposed mechanism for intramitochondrial 4-HNE production through $H_2O_2$-mediated $L_4CL$ peroxidation downstream MAO-A. Data are expressed as means ± sem (*$p < 0.05$, **$p < 0.01$ vs WT mice).

made of four linoleic moieties, the main precursor of 4-HNE. Consequently, we observed an increase in 12(S), 13(S), and 9(S) species of HODEs, which are different oxidation products of linoleic acid (Fig. 1f). Our results indicate that MAO-A-dependent ROS generation promotes intramitochondrial formation of 4-HNE through $L_4CL$ peroxidation and HODEs intermediate formation (Fig. 1g).

## MitoALDH2 mitigates MAO-A-induced cardiac dysfunction

In order to evaluate if 4-HNE could mediate the deleterious effects of MAO-A, we overexpressed mitochondrial ALDH2, the main enzyme for 4-HNE detoxification, in hearts of MAO-A Tg mice using a cardiotropic AAV9-ALDH2 (Fig. 2a). Major 4-HNE detoxification systems were inhibited in Tg hearts, as shown by a decrease in cardiac glutathione (GSH) content and mitochondrial ALDH2 activity

(Fig. 2b, c). As expected, AAV9-ALDH2 restored basal level of ALDH2 activity and reduced 4-HNE accumulation in MAO-A Tg hearts (Fig. 2d–f). Importantly, this effect of ALDH2 was associated with a reduction in reactive hypertrophy and interstitial fibrosis (Fig. 2e–h). An improved cardiac function was also observed in AAV9-ALDH2 Tg mice compared with AAV9-GFP Tg mice, as demonstrated by the echocardiographic data (Fig. 2i, j and Table 1). These results show that mitochondrial ALDH2 protects from MAO-A-induced 4-HNE accumulation and cardiac dysfunction in MAO-A Tg.

## MAO-A-induced 4-HNE accumulation alters mitochondrial function

As we demonstrated that mitochondrial 4-HNE mediated the deleterious effects of MAO-A, we next sought to investigate by which downstream mechanisms this
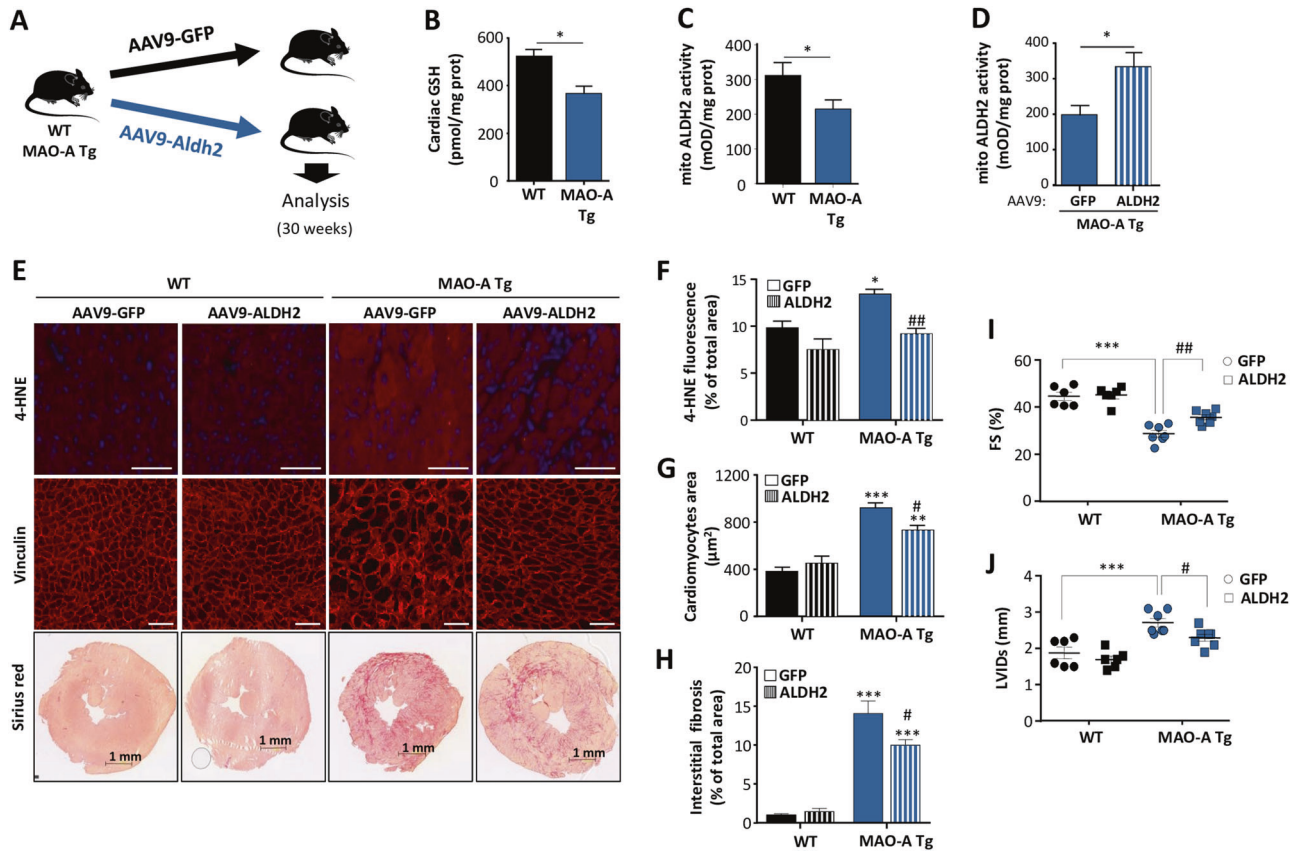
**Fig. 2 4-HNE-mediated adverse remodeling in MAO-A Tg hearts is prevented by ALDH2 gene transduction. a** Model of AAV9-GFP or AAV9-ALDH2 ($3 \times 10^{11}$ vg/mouse) transduction in WT or MAO-A Tg mice. **b** Cardiac GSH content and **c** mitochondrial ALDH2 activity in WT and MAO-A Tg hearts at 12 weeks ($n = 4$). **d** Mitochondrial ALDH2 activity on cardiac homogenates of MAO-A Tg mice after AAV9 transduction ($n = 7$). **e** 4-HNE (Scale Bar = 100 μm) and Vinculin (Scale Bar = 50 μm) immunofluorescence, and interstitial fibrosis with Sirius Red (Scale Bar = 1 mm) on cardiac cryosections of mice after AAV9 transduction. **f** Quantification of 4-HNE fluorescence as % of total area ($n = 6$–7). **g** Quantification of cardiomyocytes area on at least 100 cells/mouse in three distinct regions of the left ventricle ($n = 6$–7). **h** Quantification of fibrosis as % of total area ($n = 4$–6). Echocardiographic measurements with (**i**) fractional shortening (%) and (**j**) systolic LV internal dimension on mice after AAV9 transduction ($n = 6$–7). Data are expressed as means ± sem (*$p < 0.05$, **$p < 0.01$, ***$p < 0.001$ vs WT GFP mice; #$p < 0.05$, ##$p < 0.01$ vs MAO-A Tg GFP mice).

**Table 1** Echocardiographic parameters of WT and MAO-A Tg mice transduced with AAV9-cTnT-GFP or AAV9-cTnT-ALDH2 (M-MODE).

| AAV9-cTnT | WT | | MAO-A Tg | |
|---|---|---|---|---|
| | GFP | ALDH2 | GFP | ALDH2 |
| No of mice | 6 | 6 | 7 | 7 |
| IVSs (cm) | 0.18 ± 0.01 | 0.17 ± 0.004 | 0.16 ± 0.01*** | 0.15 ± 0.003** |
| LVIDs (cm) | 0.19 ± 0.02 | 0.17 ± 0.01 | 0.27 ± 0.01*** | 0.23 ± 0.01# |
| LVIDd (cm) | 0.34 ± 0.02 | 0.31 ± 0.01 | 0.38 ± 0.01 | 0.36 ± 0.01 |
| LVPWs (cm) | 0.16 ± 0.01 | 0.19 ± 0.01 | 0.15 ± 0.01 | 0.17 ± 0.01 |
| EDV (ml) | 0.10 ± 0.01 | 0.08 ± 0.01 | 0.14 ± 0.01 | 0.12 ± 0.01 |
| ESV (ml) | 0.020 ± 0.004 | 0.013 ± 0.002 | 0.053 ± 0.006*** | 0.036 ± 0.003# |
| EF (%) | 81.8 ± 1.7 | 82.5 ± 1.5 | 62.1 ± 2.2*** | 72.0 ± 1.4**,## |
| FS (%) | 44.6 ± 1.7 | 45.2 ± 1.5 | 28.7 ± 1.4*** | 35.7 ± 1.1**,## |
| HR (bpm) | 596 ± 12 | 571 ± 8 | 621 ± 9 | 620 ± 10 |

*IVSs* systolic LV interventricular septal thickness, *LVIDs* systolic LV internal dimension, *LVIDd* diastolic LV internal dimension, *LVPWs* systolic LV posterior wall thickness, *LVPWs* systolic LV posterior wall thickness, *EDV* end-diastolic volume, *ESV* end-systolic volume, *EF* ejection fraction, *FS* fractional shortening, *HR* heart rate

**$p < 0.01$, ***$p < 0.001$ vs corresponding WT mice

#$p < 0.05$, ##$p < 0.01$ vs AAV9-GFP for MAO-A Tg mice

occurred. Quantitative mass spectrometry-based (nanoLC-MS/MS) proteomic study after immunoprecipitation with an anti-4-HNE antibody identified 53 proteins enriched at least twofold in MAO-A Tg vs WT cardiomyocytes, with a cutoff $p$ value < 0.05 (Table 2). The majority of proteins were mitochondrial, confirming the existence of an organelle-specific regulation of 4-HNE downstream MAO-A. Analysis of overrepresented networks of 4-HNE-bound proteins with Reactome (https://reactome.org/) identified five major pathways that belong to mitochondrial metabolism (respiratory electron transport, citric acid cycle), mitoCa$^{2+}$ transport, glucose metabolism, and muscle contraction (Supplementary Fig. 2). We thus assessed the functional relevance of these pathways in response to MAO-A/4-HNE axis in AMCMs of WT mice. Activation of MAO-A with Tyr altered mitochondrial respiration, as shown by the impairment in OCR, an effect prevented with the selective MAO-A inhibitor moclobemide and with Alda-1, an allosteric activator of ALDH2 (Fig. 3a, b and Supplementary Fig. 3A–D). Interestingly, direct application of 4-HNE on AMCMs was sufficient to impair mitochondrial respiration (Supplementary Fig. 4). A decrease in ATP concentration was observed after Tyr stimulation, and this effect was prevented by Moclobemide and Alda-1 (Fig. 3c). MAO-A activation also decreased NAD+/NADH ratio and altered mitochondrial membrane potential but not in the presence of Moclobemide and Alda-1 (Fig. 3d, e). Altogether, our data show that mitochondrial 4-HNE mediates the deleterious effects of MAO-A on mitochondrial function.

## MAO-A/4-HNE axis induces mitochondrial Ca$^{2+}$ accumulation

Because mitoCa$^{2+}$ handling proteins were identified as potential 4-HNE targets (Supplementary Fig. 2), we measured the effects of MAO-A/4-HNE on mitoCa$^{2+}$. Cardiomyocytes or mitochondria of MAO-A Tg mice showed elevated levels of mitoCa$^{2+}$ compared with WT mice, as shown by the colocalization of the fluorescent probe Rhod-2-AM with MitoTracker (Fig. 4a–c). Interestingly, activation of MAO-A with Tyr in WT AMCMs or mitochondria induced mitoCa$^{2+}$ accumulation, an effect prevented with moclobemide or Alda-1 (Fig. 4d–f).

MitoCa$^{2+}$ uptake is regulated at different levels. It is driven by close interactions between the endoplasmic reticulum (ER) and the mitochondria called MAMs, resulting in the transfer of Ca$^{2+}$ through the outer membrane by VDACs, followed by the accumulation Ca$^{2+}$ into the matrix via the MCU on the inner membrane [18].

**Table 2** List of 53 4-HNE-bound proteins in cardiomyocytes of MAO-A Tg mice compared with WT mice (cutoff ratio > 2 and $p$ value < 0.05).

| Proteins | MW (kDa) | Fold change | $t$-test |
|---|---|---|---|
| Astn2 | 99.9 | 15.6 | 4.96E−05 |
| COX2 | 26.0 | 4.9 | 4.20E−05 |
| Ces1d | 61.8 | 4.6 | 1.10E−03 |
| Myh11 | 223.4 | 4.5 | 1.05E−02 |
| Bcam | 21.1 | 4.4 | 2.59E−03 |
| Col6a4 | 250.8 | 4.2 | 1.04E−02 |
| Tmx1 | 14.3 | 3.6 | 3.52E−02 |
| Hk1 | 108.3 | 3.2 | 9.82E−04 |
| Macrod1 | 35.3 | 3.1 | 6.89E−05 |
| COX3 | 29.9 | 3.1 | 7.27E−04 |
| Sdha | 72.6 | 3.0 | 8.69E−08 |
| Cox4i1 | 19.5 | 2.9 | 3.56E−05 |
| Actn2 | 103.9 | 2.9 | 9.13E−05 |
| Uqcrc1 | 52.8 | 2.8 | 4.60E−05 |
| Bsg | 24.1 | 2.8 | 6.66E−04 |
| Mybpc3 | 141.3 | 2.7 | 7.28E−04 |
| Vdac2 | 30.4 | 2.7 | 6.58E−04 |
| Uqcrc2 | 48.2 | 2.7 | 2.90E−05 |
| Hibadh | 35.5 | 2.6 | 6.87E−04 |
| Cox6c | 8.5 | 2.6 | 6.92E−03 |
| Glud1 | 61.3 | 2.5 | 1.43E−02 |
| Trim21 | 53.2 | 2.5 | 3.13E−02 |
| Atp1b1 | 35.2 | 2.5 | 2.72E−03 |
| Sdhb | 27.2 | 2.5 | 2.45E−05 |
| Ndufs2 | 52.6 | 2.4 | 4.56E−04 |
| Uqcrfs1 | 29.4 | 2.4 | 9.50E−04 |
| Ndufs1 | 79.7 | 2.4 | 7.22E−05 |
| Akr1b10 | 32.7 | 2.4 | 2.24E−02 |
| Ndufa10 | 40.6 | 2.3 | 8.03E−04 |
| Mdh2 | 35.6 | 2.3 | 2.64E−06 |
| Ndufs7 | 24.7 | 2.3 | 1.79E−02 |
| Coq9 | 27.9 | 2.2 | 9.89E−04 |
| Ugp2 | 55.5 | 2.2 | 9.17E−05 |
| Vdac1 | 30.7 | 2.2 | 1.37E−04 |
| Ndufa8 | 20.0 | 2.2 | 4.44E−02 |
| Bdh1 | 38.3 | 2.1 | 4.43E−05 |
| Try4 | 26.3 | 2.1 | 4.42E−04 |
| Ldha | 34.5 | 2.1 | 7.77E−05 |
| Etfdh | 61.2 | 2.1 | 3.99E−04 |
| Hibch | 43.0 | 2.1 | 4.99E−04 |
| Kdm2b | 144.9 | 2.1 | 1.60E−02 |
| Atp1a1 | 113.0 | 2.1 | 2.36E−03 |
| Sirt5 | 34.1 | 2.1 | 2.98E−03 |
| Slc16a1 | 38.2 | 2.1 | 6.76E−05 |
| Ndufa12 | 17.4 | 2.1 | 1.98E−04 |
| Akr7a2 | 40.6 | 2.1 | 3.21E−03 |
| Mdh1 | 36.5 | 2.0 | 1.02E−04 |
| Reep5 | 21.1 | 2.0 | 3.34E−04 |
| Atp2a2 | 109.8 | 2.0 | 4.65E−02 |
| Got2 | 47.4 | 2.0 | 8.99E−07 |
| Aldoa | 39.3 | 2.0 | 1.29E−05 |
| Aldh4a1 | 61.8 | 2.0 | 2.96E−04 |
| Aco2 | 85.5 | 2.0 | 4.66E−06 |
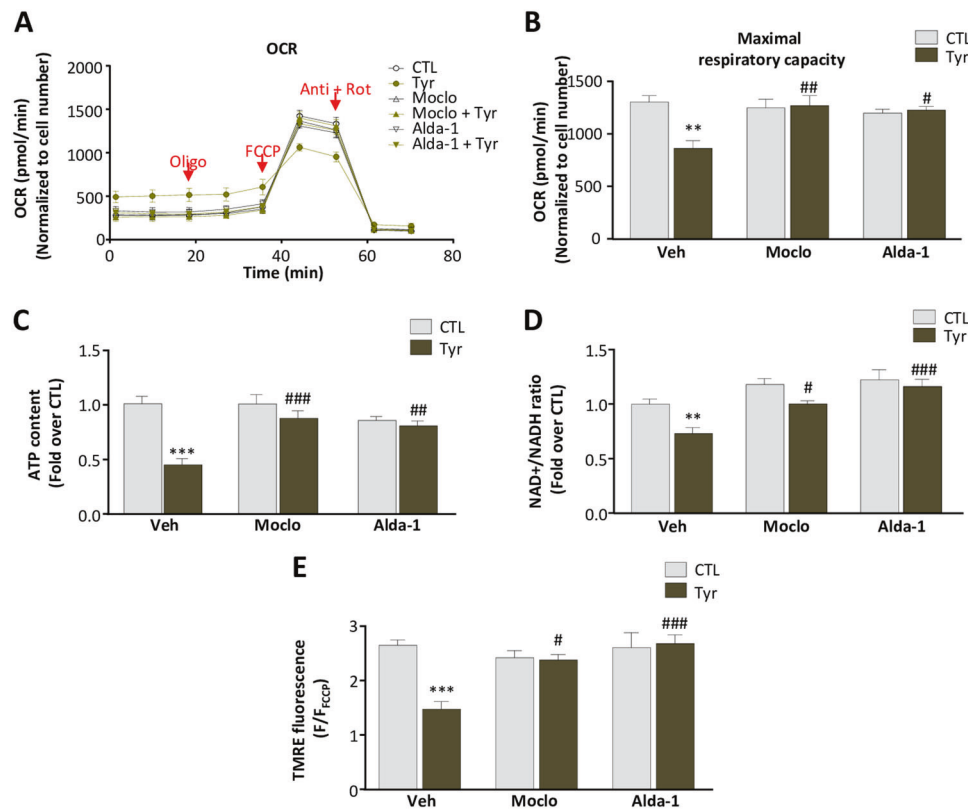
**Fig. 3 Mitochondrial MAO-A/4-HNE axis impairs organelle function. a** Oxygen consumption rate (OCR) measurements in AMCMs of WT mice treated with Tyr (50 μM, 3 h) in the presence of Moclo (15 μM) or Alda-1 (100 μM) at baseline and after addition of Oligomycin, FCCP, and Antimycin A + Rotenone ($n = 6$). **b** Maximal respiratory capacity measured from oxygen consumption rate (OCR) ($n = 6$). **c** ATP content in AMCMs isolated from WT mice stimulated with Tyr (50 μM, 3 h) in the presence of Moclo (15 μM) or Alda-1 (100 μM) ($n = 6$). **d** NAD+/NADH ratio in mitochondria isolated from WT mice and treated with Tyr (50 μM, 3 h) in the presence of Moclo (15 μM) or Alda-1 (100 μM) ($n = 5$). **e** TMRE fluorescence normalized to fluorescence in the presence of FCCP (F/F$_{FCCP}$), in AMCMs isolated from WT mice stimulated with Tyr (50 μM, 3 h) in the presence of Moclo (15 μM) or Alda-1 (100 μM) ($n = 6$). Data are expressed as means ± sem (**$p < 0.01$, ***$p < 0.001$ vs CTL; #$p < 0.05$, ##$p < 0.01$, ###$p < 0.001$ vs Tyr).

As observed in the proteomic study, an increased association between VDAC1 and 4-HNE was shown by co-immunoprecipitation experiments in AMCMs stimulated with Tyr (Fig. 5a). We evaluated the interactions between ER and mitochondria, which involve associations of VDAC1, IP3R1, and GRP75. PLA showed that AMCMs of MAO-A Tg mice displayed increased interactions between VDAC1/IP3R1, VDAC1/GRP75, and IP3R1/GRP75 compared with WT mice, potentially favoring Ca²⁺ transfer (Fig. 5b–e). Interestingly, in WT AMCMs, histamine, a known stimulator of IP3R-mediated Ca²⁺ transfer from ER to mitochondria, enhanced Tyr-induced mitoCa²⁺ accumulation (Fig. 5f, g). On the other hand, Xestospongin C, a specific inhibitor of IP3R, reduced Tyr-mediated mitoCa²⁺transfer (Fig. 5f, g). Thus, MAO-A/4-HNE axis may potentiate Ca²⁺ transfer through increased interactions between ER and mitochondria and enhanced Ca²⁺ outer membrane transfer through VDAC1.

## 4-HNE binding to MCU induces MitoCa²⁺ overload and mitochondrial dysfunction

Ca²⁺ transport through the inner membrane occurs via the MCU, which is regulated by its two main partners MICU1 and MICU2 [19]. We investigated whether MCU also participated in mitoCa²⁺ accumulation in response to MAO-A/4-HNE. Tyr-mediated mitoCa²⁺ accumulation was significantly reduced by the MCU inhibitor Ru360, in both isolated WT AMCMs and purified mitochondria (Fig. 4e, f). In line with these findings, direct application of 4-HNE on AMCMs promoted mitoCa²⁺ accumulation, an effect inhibited by RU360 (Fig. 6a). This finding prompted us to determine whether MCU, MICU1, or MICU2 were potential targets of 4-HNE covalent binding. In AMCMs of MAO-A Tg mice, immunoprecipitation assays showed that 4-HNE levels increased on MCU, but not on MICU1 and MICU2 (Fig. 6b and Supplementary Fig. 5A). In NRVMs treated with Tyr, we also found increased association of
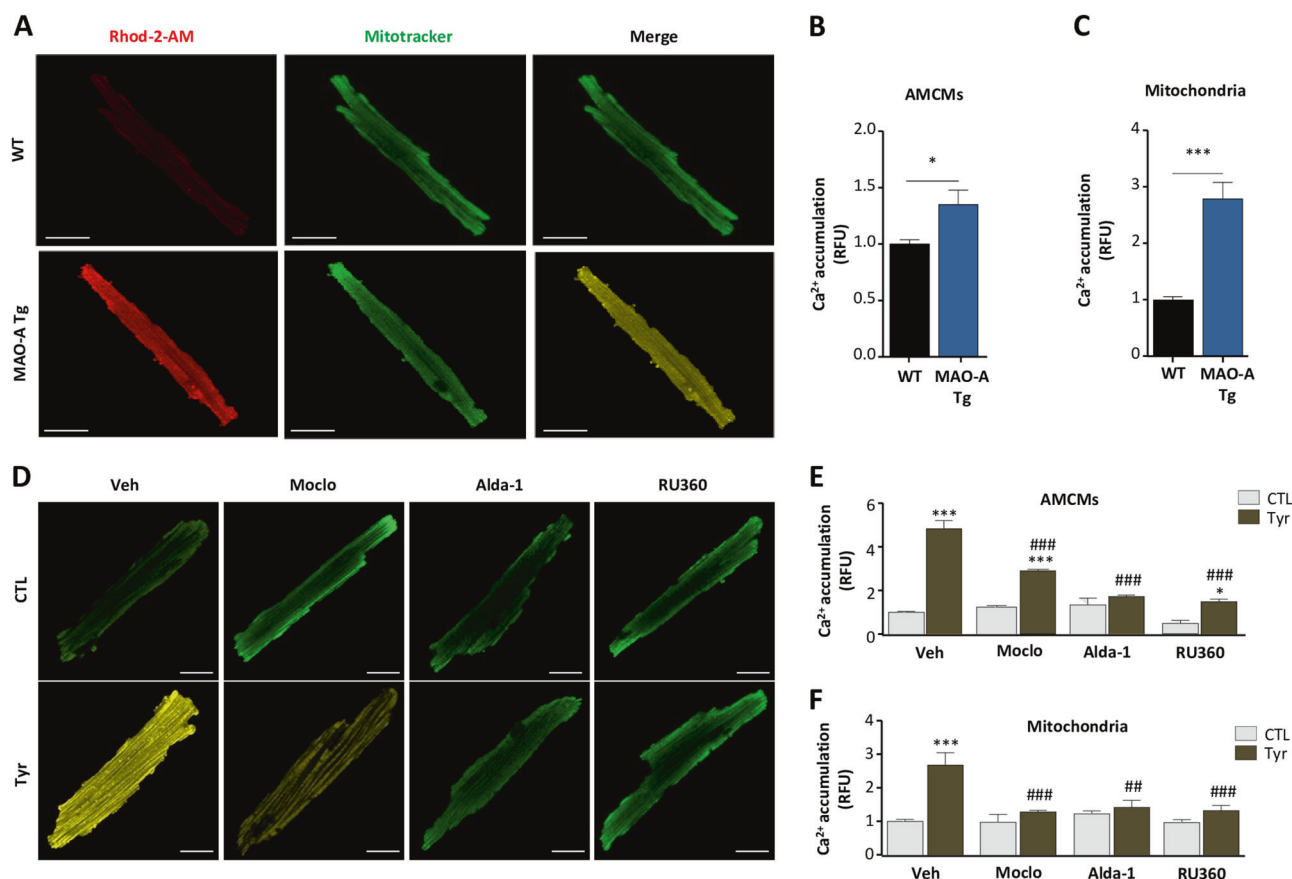
**Fig. 4 MAO-A activation induces 4-HNE-dependent increase in mitoCa$^{2+}$ levels. a** Representative images of mitochondrial Ca$^{2+}$ (mitoCa$^{2+}$) accumulation in WT or MAO-A Tg AMCMs. The Ca$^{2+}$ fluorescent probe Rhod-2-AM overlapped with the mitochondrial marker Mitotracker green. Quantification of mitoCa$^{2+}$ accumulation in AMCMs (**b**) and isolated mitochondria (**c**) of MAO-A Tg mice ($n = 5–6$). **d, e** Representative images and quantification of mitoCa$^{2+}$ accumulation in AMCMs of WT mice treated with Tyr (50 µM, 3 h) in the presence of Moclo (15 µM), Alda-1 (100 µM), or RU360 (10 µM) ($n = 5–6$). **f** Quantification of Ca$^{2+}$ accumulation in isolated mitochondria of WT mice treated with Tyr (50 µM, 30 min) ($n = 5–6$). Data are expressed as means ± sem (*$p < 0.05$, ***$p < 0.001$ vs Veh or WT; ##$p < 0.01$, ###$p < 0.001$ vs MI WT or Tyr).

MCU and 4-HNE, but not MICU1 or MICU2 (Fig. 6c and Supplementary Fig. 5B). In order to better understand how 4-HNE adducts could modify MCU-mediated Ca$^{2+}$ uptake, we evaluated MCU complex formation, the active form of the channel. Indeed, the MCU per se is not able to form the channel but should organize in oligomers allowing efficient mitoCa$^{2+}$ uptake [20, 21]. Size-exclusion chromatography followed by western blot on NRVMs showed that MCU was eluted and detected in a high molecular weight fraction (F1 ≈ 400 kDa) only in the Tyr-stimulated condition, which corresponded to higher-order oligomers (Fig. 6d). Furthermore, in nonreducing western blots conditions, MAO-A Tg cardiomyocytes displayed larger MCU complexes compared with WT (Fig. 6e). Similar findings were observed in NRVMs treated with Tyr or 4-HNE (Fig. 6f and Supplementary Fig. 5C, D). Importantly, Alda-1 prevented MCU oligomerization, confirming the role of 4-HNE in MAO-A-induced MCU conformational modifications (Fig. 6f). In order to assess if MCU functionally regulated mitochondrial

function in response to MAO-A activation, we incubated WT AMCMs with Tyr in the presence of the MCU inhibitor RU360. Seahorse measurements indicated that respiration impairment induced by MAO-A could be prevented with RU360 (Fig. 6g, h and Supplementary Fig. 6). Loss of ATP content and mitochondrial membrane depolarization induced by MAO-A were also partially reduced in the presence of RU360 in WT AMCMs (Fig. 6i, j). Altogether, these results identify for the first time MAO-A as a regulator of MCU channel through 4-HNE-mediated conformational changes and show that MCU activation participates in mitochondrial dysfunction.

## MAO-A inactivation protects from 4-HNE accumulation and cardiac remodeling during chronic ischemia

In order to evaluate the pathophysiological relevance of our findings, we developed a model of MI induced by
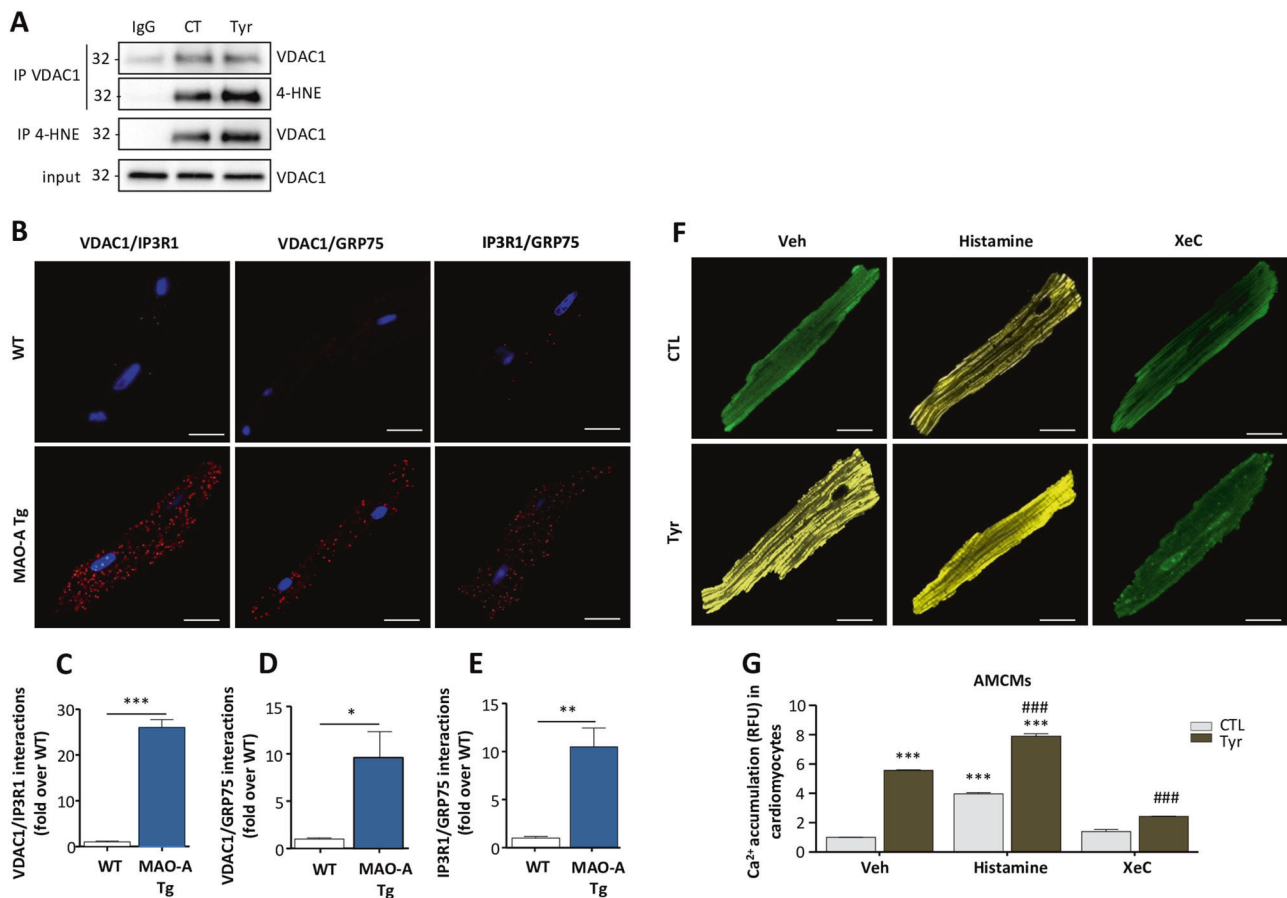
**Fig. 5 Implication of MAMs in MAO-A-induced mitoCa²⁺ increase. a** Representative immunoblots showing the interaction of 4-HNE with VDAC1 in NRVMs stimulated with Tyr. Immunoprecipitation (IP) experiments were performed with 4-HNE or VDAC1 antibodies. IgG was used as a negative control for IP. Input is a control of cell lysates $n = 4$. **b** Representative images of in situ interactions (red fluorescent dots) between IP3R1 and GRP75 or IP3R1 and VDAC1 or GRP75 and VDAC1 in WT or MAO-A Tg cardiomyocytes. Nuclei are stained with DAPI. Scale bar, 20 μm. **c–e** Quantifications of the proximity ligation assay ($n = 3$). **f** Representative images of mitoCa²⁺ accumulation in AMCMs of WT mice treated with Tyr and challenged with histamine (100 μM) or Xestospongin C (2 μM). **g** Quantifications of mitoCa²⁺ accumulation ($n = 5$). Data are expressed as means ± sem (*$p < 0.05$, **$p < 0.01$, ***$p < 0.001$ vs WT or Veh, ###$p < 0.001$ vs Tyr).

permanent coronary artery ligation in mice. Four weeks post-MI, while ALDH2 expression remained unchanged, both MAO-A levels and 4-HNE-bound proteins were elevated compared with sham-operated mice (Fig. 7a). The same observation was made in ventricular samples of human ischemic cardiomyopathy (Fig. 7b). In order to test if MAO-A/4-HNE axis could be associated with chronic cardiac remodeling, mice were treated with the selective and reversible MAO-A inhibitor, moclobemide (20 mg/kg/day), after the surgery and the treatment was sustained during 4 weeks (Fig. 7c). Moclobemide efficiently inhibited MAO-A activity and reduced 4-HNE accumulation post-MI (Fig. 7d, Supplementary Fig. 7A). This was accompanied by reduced cardiac remodeling, as shown by improved ejection fraction, reduced ventricular dilatation, decreased heart-to-body weight ratios, and lung edema (Fig. 7e, Table 3 and Supplementary Fig. 7D, E). In order to test if cardiomyocytes were the primary cells responsible for these

effects, we used mice with cardio-selective deletion of MAO-A (*Maoa*fl crossed with *αMHC-Cre*⁺ mice) (Supplementary Fig. 7B, C). Cardiomyocyte-specific deletion of MAO-A reduced 4-HNE accumulation and mitigated contractility impairment and dilatation at 4 weeks post-MI (Fig. 7d, e, Supplementary Fig. 7G, H and Table 3). Heart-to-body weight ratios and lung congestions were also reduced in MAO-A cKO mice compared with WT mice (Supplementary Fig. 7D, E). To evaluate the volume of the scar zone, we performed 3D-whole heart imaging using high-resolution LSFM. As shown by 3D reconstructions in Fig. 7f, the scar zone (blue) represented 14% of total heart in WT mice while it was reduced to 5% in MAO-A cKO mice, suggesting that MAO-A deletion limited expansion of the infarct (Supplementary Fig. 7F). These results were confirmed with Masson's Trichrome showing a marked decrease in the scar area of MAO-A cKO hearts compared with WT (Fig. 7f and Supplementary Fig. 7F).
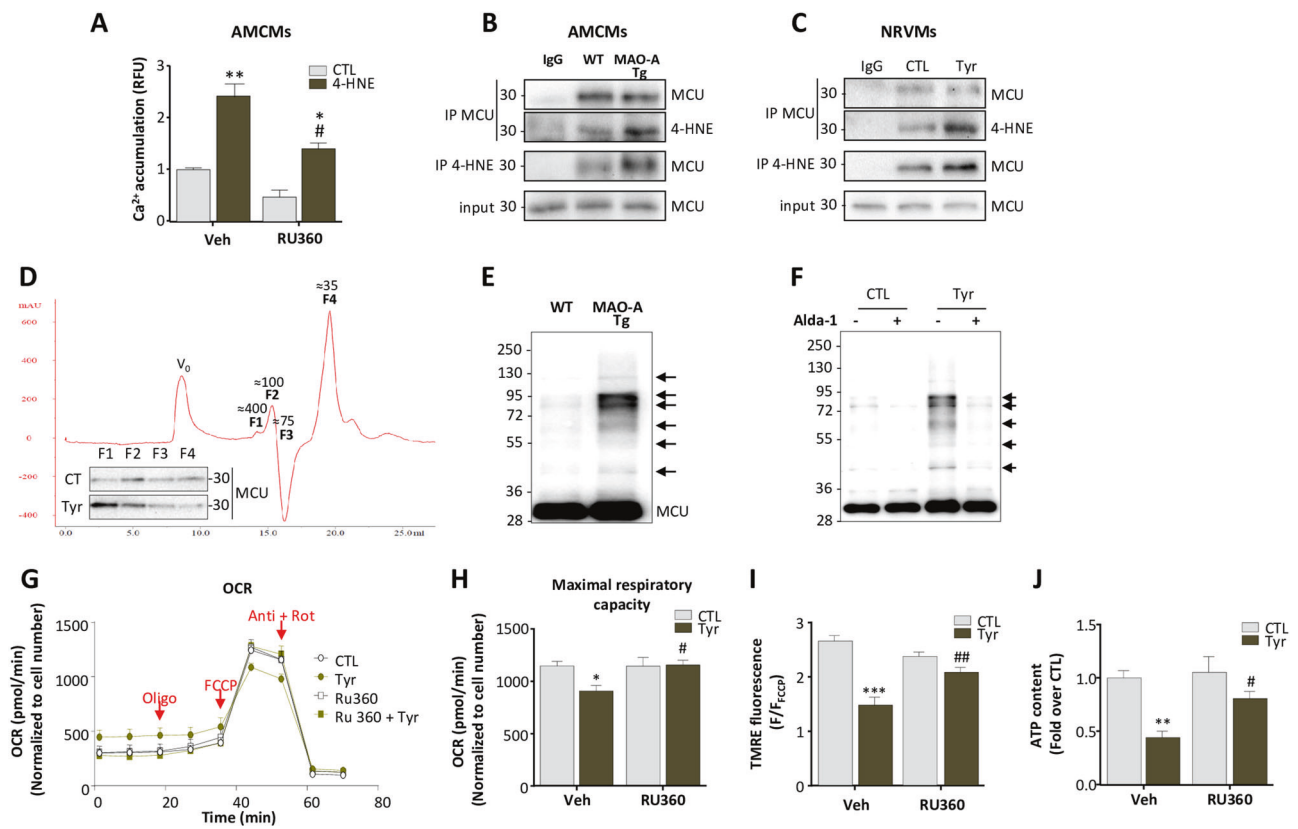
**Fig. 6 MAO-A/4-HNE axis regulates mitoCa²⁺-induced mito-chondrial dysfunction through MCU-binding and higher-order complex formation. a** Quantifications of mitoCa²⁺ accumulation in AMCMs isolated from WT mice treated with 4-HNE (5 µM, 15 min) in the presence of RU360 (10 µM) $n = 4$. Representative immunoblots showing the interaction of 4-HNE with MCU (**b**) in AMCMs of MAO-A Tg mice, (**c**) in NRVMs stimulated with Tyr (500 µM, 1 h). Immunoprecipitation (IP) experiments were performed with 4-HNE or MCU antibodies. IgG was used as a negative control for IP. Input is a control of cell lysates $n = 4$. **d** Representative elution profile and immunoblots showing MCU expression in different protein complexes obtained after size-exclusion chromatography (SEC) of nondenatured NRVMs lysates using HPLC, after stimulation with Tyr (500 µM, 4 h). The elution profile of molecular complexes is shown in four different fractions (F1–F4) with estimated sizes: F1 at ≈400 kDa, F2 at ≈100

kDa; F3 at ≈75 kDa and F4 at ≈35 kDa. Representative nonreducing immunoblots showing MCU higher-order complex formation (**e**) in AMCMs of MAO-A Tg mice and (**f**) in NRVMs stimulated with Tyr in the presence of Alda-1 (100 µM). **g** Oxygen consumption rate (OCR) measurements in AMCMs of WT mice treated with Tyr (50 µM, 3 h) in the presence of RU360 (10 µM) at baseline and after addition of Oligomycin, FCCP and Antimycin A + Rotenone ($n = 5$–6). **h** Oxygen consumption rate (OCR) associated with maximal respiratory capacity ($n = 5$–6). **i** TMRE fluorescence normalized to fluorescence in the presence of FCCP (F/F_FCCP) in AMCMs of WT mice stimulated with Tyr (50 µM, 3 h) in the presence of RU360 (10 µM) ($n = 6$). **j** ATP content in AMCMs of WT mice stimulated with Tyr (50 µM, 3 h) in the presence of RU360 (10 µM) ($n = 6$). Data are expressed as means ± sem (*$p < 0.05$, **$p < 0.01$, ***$p < 0.001$ vs CTL; #$p < 0.05$, vs 4-HNE or Tyr).

Histologically, MAO-A cKO hearts had lessened reactive hypertrophy in the remote zone of the infarct compared with WT mice (Fig. 7g) while interstitial fibrosis was slightly decreased (Supplementary Fig. 7G–I). Next, we evaluated if the newly identified mechanism of action of 4-HNE on MCU/mitoCa²⁺ was dysregulated in ischemic remodeling. Most interestingly, we observed a co-immunoprecipitation of 4-HNE with MCU in MI hearts, associated with MCU oligomer formation, and this was inhibited by moclobemide (Fig. 7h, i). Moreover, cardiac mitochondria of ischemic hearts displayed higher mitoCa²⁺ levels compared with SHAM mice, and this effect was attenuated in MAO-A cKO mice (Fig. 7j). Altogether, these results strongly support a

role for cardiac MAO-A in the generation of deleterious 4-HNE and MCU-mediated Ca²⁺ overload during chronic remodeling.

## Discussion

In this study, we show for the first time that overactivation of MAO-A leads to intramitochondrial generation of 4-HNE with functional consequences on mitoCa²⁺ transport, mitochondrial dysfunction, and chronic ventricular remodeling post-MI (Fig. 8). To our knowledge, this constitutes the first evidence of a link between MAO-A activation
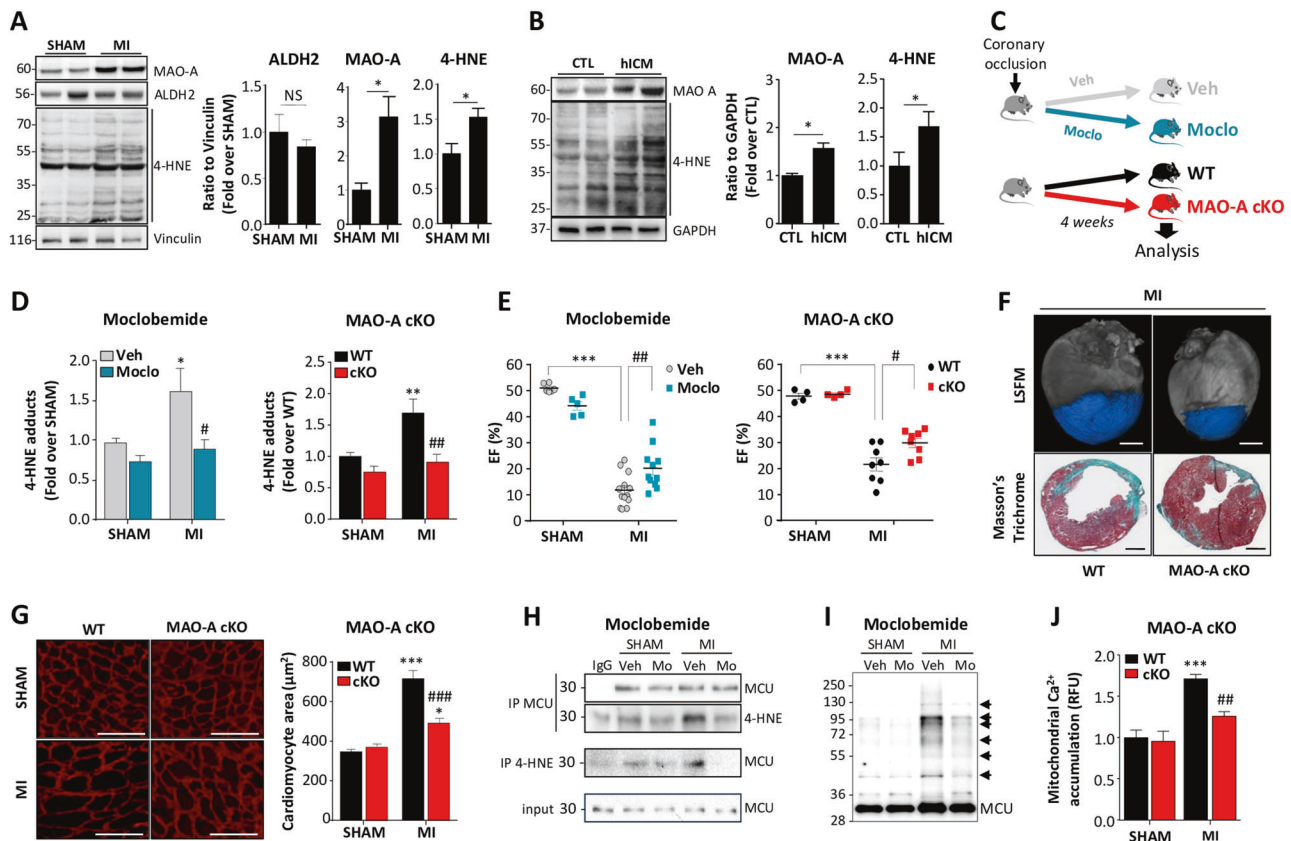
**Fig. 7 Effect of Moclobemide or MAO-A deficiency on myocardial infarction (MI)-induced 4-HNE accumulation and cardiac remodeling.** Immunoblots and quantifications of ALDH2, MAO-A, and 4-HNE protein adducts in (**a**) cardiac homogenates of SHAM or MI mice ($n = 4$) and (**b**) left ventricular myocardium of CTL ($n = 4$) or human ischemic cardiomyopathy patients (hICM) ($n = 5$). **c** Model of MI experiments with moclobemide treatment (20 mg/kg/day) or in mice with deletion of MAO-A in cardiomyocytes (MAO-A cKO). **d** Quantifications of 4-HNE protein adducts in mouse hearts after MI. (MAO cKO: $n = 4$ sham, $n = 8$ MI; Moclobemide: $n = 5$ sham, $n = 5$ MI). **e** Echocardiographic parameters of Ejection Fraction (EF, %). **f** Representative pictures of 3D-reconstructed hearts by LSFM with scar zone in blue in upper panel (Scale Bar = 2 mm) or Masson's

Trichrome staining in lower panel (Scale Bar = 1 mm). **g** Vinculin (Scale Bar = 50 µm) immunofluorescence staining with quantifications of mean cardiomyocyte area. (MAO-A cKO: $n = 4$ sham, $n = 8$ MI). **h** Immunoprecipitation experiments with MCU or 4-HNE in heart homogenates of mice subjected to 4 weeks ischemia (MI) in the presence of moclobemide (20 mg/kg/day) ($n = 3$ per group). **i** Representative nonreducing immunoblots showing MCU higher-order complex formation in heart homogenates of mice subjected to 4 weeks ischemia (MI) in the presence of moclobemide (20 mg/kg/day) ($n = 3$ per group). **j** Quantification of Ca²⁺ accumulation in isolated mitochondria of WT and MAO-A cKO mice subjected to 1 week ischemia ($n = 5$–7).

during cardiac injury and the previously recognized deleterious effects of 4-HNE. Recently, it has been shown that human end-stage ischemic hearts displayed an increase in MAO-A and MAO-B activities, but the causative role of these enzymes in the pathogenesis of chronic ischemic remodeling and the associated mechanisms were not investigated [22]. Here, we show that pharmacological or genetic inhibition of MAO-A reduces deleterious remodeling in mice with coronary artery ligation. The role of MAO-A has been previously demonstrated in acute ischemia/reperfusion injury [23] and in pressure overload-induced cardiac remodeling [24]. Its mechanisms of action have been delineated in a mouse model of MAO-A overexpression that, despite high MAO-A expression levels, is useful in deciphering specific pathways downstream

MAO-A [25]. However, previous studies mainly focused on the mechanisms of action of H₂O₂. Recently, Kaludercic et al. suggested a role for aldehydes in MAO-B-induced deleterious effects, showing a worsening effect of in vitro ALDH2 inhibition after dopamine treatment [26]. Here, we unravel for the first time that lipid-derived aldehydes, in particular the most abundant 4-HNE, act downstream MAO-A to mediate mitochondria dysfunction. Mounting evidence has linked lipid peroxidation aldehydes such as 4-HNE with various human pathological states [8] and with mice models of HF [10]. However, the mechanisms of 4-HNE mitochondrial accumulation as well as the identification of its mitochondrial targets remained poorly understood [27]. Here, we show that MAO-A is one of the factors driving 4-HNE mitochondrial accumulation through L₄CL

**Table 3** Echocardiographic parameters of mice treated with Moclobemide (20 mg/kg/d) or MAO-A cKO mice 4 weeks after myocardial ischemia (2D imaging).

| | SHAM | | MI | |
|---|---|---|---|---|
| | Vehicle | Moclobemide | Vehicle | Moclobemide |
| $N$ | 6 | 5 | 13 | 11 |
| Ad, mm$^2$ | 24.3 ± 1.2 | 26.6 ± 0,6 | 43.7 ± 1.6*** | 38.1 ± 2.3**,# |
| EDV, ml | 0.068 ± 0.005 | 0.077 ± 0.002 | 0.199 ± 0.093*** | 0.15 ± 0.01***,## |
| As, mm$^2$ | 15.7 ± 0.7 | 19.0 ± 0.6 | 40.4 ± 1.7*** | 32.95 ± 2.25***,## |
| ESV, ml | 0.033 ± 0.002 | 0.045 ± 0.002 | 0.170 ± 0.012*** | 0.125 ± 0.014***,# |
| EF (%) | 50.7 ± 0.7 | 43.9 ± 1.6 | 11.7 ± 1.7*** | 20.0 ± 2.5***,## |
| HR, bpm | 479.38 ± 12.61 | 398.49 ± 6.88* | 503.79 ± 18.65 | 470.66 ± 15.91 |

| | SHAM | | MI | |
|---|---|---|---|---|
| | WT | MAO-A cKO | WT | MAO-A cKO |
| $N$ | 4 | 4 | 8 | 8 |
| Ad, mm$^2$ | 26.10 ± 0.97 | 29.45 ± 0.98 | 49.94 ± 3.15*** | 37.82 ± 1.69*,## |
| EDV, ml | 0.078 ± 0.005 | 0.073 ± 0.018 | 0.234 ± 0.025*** | 0.151 ± 0.012*,# |
| As, mm$^2$ | 12.5 ± 2.5 | 17.5 ± 2.5 | 42.9 ± 3.6*** | 32.5 ± 1.6***,# |
| ESV, ml | 0.030 ± 0.004 | 0.035 ± 0.006 | 0.188 ± 0.023*** | 0.106 ± 0.010*,## |
| EF (%) | 47.5 ± 1.2 | 48.3 ± 0.6 | 21.2 ± 2.2*** | 29.5 ± 1.8***,# |
| HR, bpm | 500.25 ± 22.93 | 460.75 ± 14.59 | 540.13 ± 21.17 | 466.78 ± 21.52 |

*Ad* end-diastolic area, *EDV* end-diastolic volume, *As* end-systolic area, *ESV* end-systolic volume, *EF* ejection fraction, *HR* Heart rate

**$p < 0.01$, ***$p < 0.001$ vs. corresponding SHAM mice

#$p < 0.05$, ##$p < 0.01$ vs. mice treated with Vehicle or WT mice for MI condition
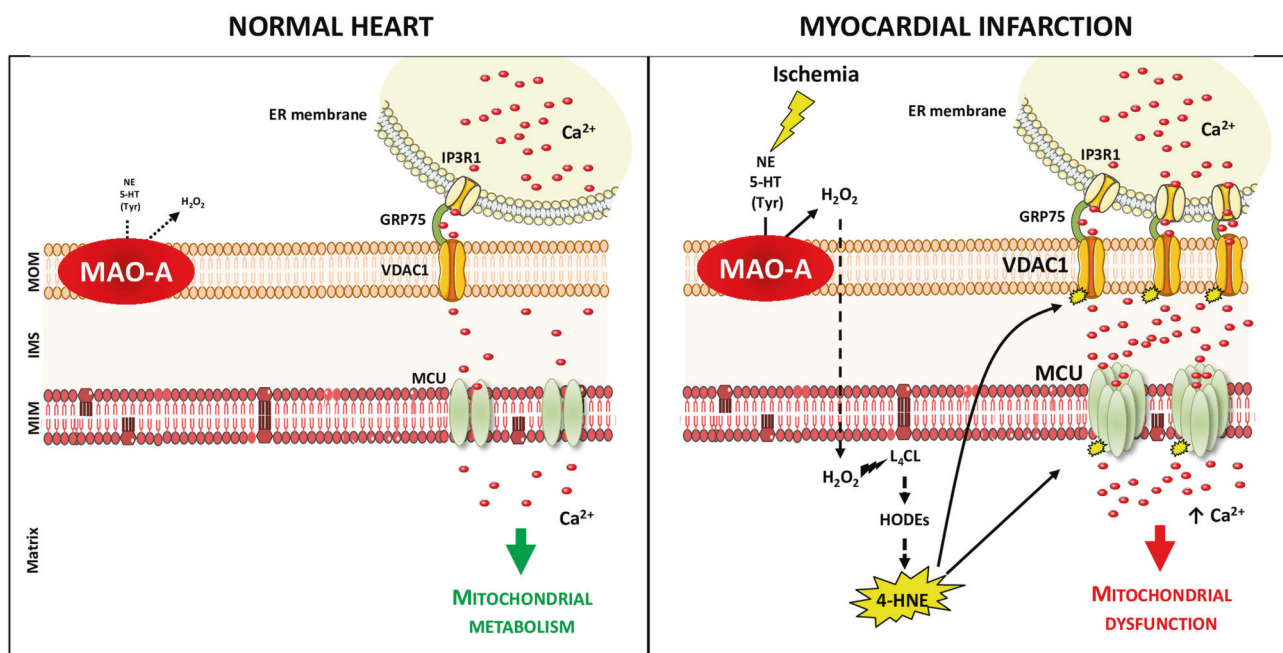


**Fig. 8** Schema illustrating the mechanisms associated with MAO-A/4-HNE signaling during chronic ischemia (right panel) compared with normal conditions (left panel).

peroxidation. The loss of L$_4$CL in mitochondrial membrane constitutes a hallmark of cardiomyopathy, with consequences on the enzymatic activity of cytochrome c oxidase and respiratory capacity [28]. However, this alteration of L$_4$CL is not sufficient to explain the mitochondrial dysfunction observed with MAO-A, as ALDH2 activation conferred significant protection. This indicates that 4-HNE mitochondrial accumulation plays a major role in MAO-dependent mitochondrial damage.

Our results also put forward that 4-HNE acts at its site of formation since: (i) 4-HNE accumulates within the mitochondria after MAO activation, (ii) overexpression of ALDH2 activity, a mitochondrial enzyme, rescues MAO-A-mediated HF; (iii) mass spectrometry of 4-HNE-bound proteins shows overrepresentation of mitochondrial proteins. The main pathways identified by proteomic study were "mitochondrial metabolism, glucose metabolism, mitoCa$^{2+}$ transport, and muscle contraction". Interestingly, two targets of 4-HNE (NDUFS2, SDHA) were also found in large-scale analysis of 4-HNE-bound proteins in doxorubicin-induced cardiomyopathy, which suggests the existence of common targets in stressed cardiomyocytes [29].

Due to its key role in bioenergetics, redox homeostasis and cell death, mitochondrial dysfunction is a critical factor in the development and progression of HF [1]. Of particular interest, mitoCa$^{2+}$ overload seems to be an important determinant of ischemic ventricular remodeling. A recent study showed that blockade of mitoCa$^{2+}$ extrusion by NCX channel promoted infarct expansion and death of border cardiomyocytes [4]. Santelli et al. also demonstrated that leaky Ryr2 caused mitoCa$^{2+}$ overload and dysfunction in HF [5]. Interestingly, mitoCa$^{2+}$ amounts were lessened in MAO-A cKO mice compared with WT after ischemia, which was associated with a better cardiac function, identifying MAO-A as an activator of mitoCa$^{2+}$ entry. In addition, direct 4-HNE treatment led to mitoCa$^{2+}$ overload and mitochondrial dysfunction in both isolated cardiomyocytes and mitochondria. The mechanism by which Ca$^{2+}$ overload induces mitochondrial dysfunction remains incompletely understood. One hypothesis could be that mitoCa$^{2+}$ exacerbates ROS generation, further impairing mitochondrial function through the generation of superoxide due to mild uncoupling of mitochondria [4].

Of particular importance, we identified VDAC and MCU as relevant targets of 4-HNE adduct formation following MAO-A activation. The entry of Ca$^{2+}$ inside the mitochondria is highly regulated by the communication between the ER and the mitochondria called MAMs [18] and the association of the VDAC1/GRP75/IP3R complex [30]. MAO-A Tg mice exhibited higher levels of MAMs compared with WT mice, which could favor mitoCa$^{2+}$ entry from the ER. As we and others [31] demonstrated that

4-HNE covalently bound to VDAC1, it is possible that the carbonylated form of VDAC1 has better interactions with its partners GRP75 and IP3R1, strengthening mitoCa$^{2+}$ transfer during MAO-A activation. We also observed that MAO-A-dependant 4-HNE formation led to the formation of higher-order MCU oligomers. MCU oligomer formation is sensitive to posttranslational modifications, among which oxidation of Cys-97, resulting in persistent MCU channel activity and higher mitoCa$^{2+}$ uptake [32]. As 4-HNE exhibits the strongest reactivity for Cys residues, we can hypothesize that increased 4-HNE binding could modify MCU activity through similar conformational changes. These results put forward MAO-A as a regulator of MCU through 4-HNE-mediated posttranslational modification and subsequent conformational changes. Finally, we provide evidences that MCU-mediated mitoCa$^{2+}$ overload following MAO-A/4-HNE activation is deleterious, as mitochondrial dysfunction is prevented with the MCU inhibitor RU360. While it has been clearly demonstrated that increasing the levels of mitoCa$^{2+}$ was deleterious in pathological cardiac remodeling [4, 5], the selective inhibition of MCU has given conflicting results. Global MCU$-/-$ mice had normal response to isoproterenol or pressure overload stress [33, 34], suggesting the existence of compensatory mechanisms. On the other hand, cardiac-specific ablation of MCU in adult mice protected mice from I/R damage [35] and pharmacological inhibition of MCU was beneficial in pressure-overloaded hearts [36]. In the present study, our results highlight for the first time a deleterious role for MCU-dependent Ca$^{2+}$ overload in chronic ischemic remodeling. In conclusion, we propose a model whereby excessive activation of MAO-A in cardiac stress conditions promotes mitochondrial 4-HNE accumulation and binding on VDAC1 and MCU, both acting in a synergistic way to promote excessive mitoCa$^{2+}$ entry and mitochondrial dysfunction (Fig. 8).

Finally, our identification of MAO-A as a major source of mitochondrial 4-HNE during post-MI remodeling paves the way toward targeted therapies aimed at decreasing aldehyde load, mitoCa$^{2+}$ dysregulation and energetic depletion in HF. As the MAO-A inhibitor moclobemide is approved in Europe and used as an antidepressant, it would be interesting to consider the possibility of repurposing this drug for HF therapy.

## Compliance with ethical standards

**Conflict of interest** The authors declare that they have no conflict of interest.

**Publisher's note** Springer Nature remains neutral with regard to jurisdictional claims in published maps and institutional affiliations.

## References

1. Brown DA, Perry JB, Allen ME, Sabbah HN, Stauffer BL, Shaikh SR, et al. Mitochondrial function as a therapeutic target in heart failure. Nat Rev Cardiol. 2017;14:238–50.

2. Rizzuto R, De Stefani D, Raffaello A, Mammucari C. Mitochondria as sensors and regulators of calcium signalling. Nat Rev Mol Cell Bio. 2012;13:566–78.

3. Bertero E, Maack C. Calcium signaling and reactive oxygen species in mitochondria. Circulation Res. 2018;122:1460–78.

4. Luongo TS, Lambert JP, Gross P, Nwokedi M, Lombardi AA, Shanmughapriya S, et al. The mitochondrial Na$^+$/Ca$^{2+}$ exchanger is essential for Ca$^{2+}$ homeostasis and viability. Nature. 2017;545:93–7.

5. Santulli G, Xie WJ, Reiken SR, Marks AR. Mitochondrial calcium overload is a key determinant in heart failure. Proc Natl Acad Sci USA. 2015;112:11389–94.

6. Kornfeld OS, Hwang S, Disatnik M-H, Chen C-H, Qvit N, Mochly-Rosen D. Mitochondrial reactive oxygen species at the heart of the matter: new therapeutic approaches for cardiovascular diseases. Circulation Res. 2015;116:1783–99.

7. Gueraud F. 4-Hydroxynonenal metabolites and adducts in precarcinogenic conditions and cancer. Free Radic Bio Med. 2017;111:196–208.

8. Mak S, Lehotay DC, Yazdanpanah M, Azevedo ER, Liu PP, Newton GE. Unsaturated aldehydes including 4-OH-nonenal are elevated in patients with congestive heart failure. J Card Fail. 2000;6:108–14.

9. Chen CH, Budas GR, Churchill EN, Disatnik MH, Hurley TD, Mochly-Rosen D. Activation of aldehyde dehydrogenase-2 reduces ischemic damage to the heart. Science. 2008;321:1493–5.

10. Gomes KM, Campos JC, Bechara LR, Queliconi B, Lima VM, Disatnik MH, et al. Aldehyde dehydrogenase 2 activation in heart failure restores mitochondrial function and improves ventricular function and remodelling. Cardiovasc Res. 2014;103:498–508.

11. Kaludercic N, Mialet-Perez J, Paolocci N, Parini A, Di Lisa F. Monoamine oxidases as sources of oxidants in the heart. J Mol Cell Cardiol. 2014;73:34–42.

12. Villeneuve C, Guilbeau-Frugier C, Sicard P, Lairez O, Ordener C, Duparc T, et al. p53-PGC-1alpha pathway mediates oxidative mitochondrial damage and cardiomyocyte necrosis induced by monoamine oxidase-A upregulation: role in chronic left ventricular dysfunction in mice. Antioxid Redox Signal. 2013;18:5–18.

13. Liao C-P, Lin T-P, Li P-C, Geary LA, Chen K, Vaikari VP, et al. Loss of MAOA in epithelia inhibits adenocarcinoma development, cell proliferation and cancer stem cells in prostate. Oncogene. 2018;37:5175–90.

14. Abadie S, Jardet C, Colombelli J, Chaput B, David A, Grolleau JL, et al. 3D imaging of cleared human skin biopsies using light-sheet microscopy: a new way to visualize in-depth skin structure. Ski Res Technol. 2018;24:294–303.

15. Morel E, Marcantoni A, Gastineau M, Birkedal R, Rochais F, Garnier A, et al. cAMP-binding protein Epac induces cardiomyocyte hypertrophy. Circulation Res. 2005;97:1296–304.

16. Fazal L, Laudette M, Paula-Gomes S, Pons S, Conte C, Tortosa F, et al. Multifunctional mitochondrial Epac1 controls myocardial cell death. Circ Res. 2017;120:645–57.

17. Liu W, Porter NA, Schneider C, Brash AR, Yin HY. Formation of 4-hydroxynonenal from cardiolipin oxidation: Intramolecular peroxyl radical addition and decomposition. Free Radic Bio Med. 2011;50:166–78.

18. Giorgi C, Missiroli S, Patergnani S, Duszynski J, Wieckowski MR, Pinton P. Mitochondria-associated membranes: composition, molecular mechanisms, and physiopathological implications. Antioxid Redox Sign. 2015;22:995–1019.

19. Patron M, Checchetto V, Raffaello A, Teardo E, Reane DV, Mantoan M, et al. MICU1 and MICU2 finely tune the mitochondrial Ca2+ uniporter by exerting opposite effects on MCU activity. Mol Cell. 2014;53:726–37.

20. Tomar D, Dong Z, Shanmughapriya S, Koch DA, Thomas T, Hoffman NE, et al. MCUR1 Is a scaffold factor for the MCU complex function and promotes mitochondrial bioenergetics. Cell Rep. 2016;15:1673–85.

21. Wang Y, Nguyen NX, She J, Zeng W, Yang Y, Bai XC, et al. Structural mechanism of EMRE-dependent gating of the human mitochondrial calcium uniporter. Cell. 2019;177:1252–61 e13.

22. Manni ME, Rigacci S, Borchi E, Bargelli V, Miceli C, Giordano C, et al. Monoamine oxidase Is overactivated in left and right ventricles from ischemic hearts: an intriguing therapeutic target. Oxid Med Cell Longev. 2016;2016:4375418.

23. Pchejetski D, Kunduzova O, Dayon A, Calise D, Seguelas MH, Leducq N, et al. Oxidative stress-dependent sphingosine kinase-1 inhibition mediates monoamine oxidase A-associated cardiac cell apoptosis. Circ Res. 2007;100:41–9.

24. Kaludercic N, Takimoto E, Nagayama T, Feng N, Lai EW, Bedja D, et al. Monoamine oxidase A-mediated enhanced catabolism of norepinephrine contributes to adverse remodeling and pump failure in hearts with pressure overload. Circ Res. 2010;106:193–202.

25. Santin Y, Sicard P, Vigneron F, Guilbeau-Frugier C, Dutaur M, Lairez O, et al. Oxidative stress by monoamine oxidase-A impairs transcription factor EB activation and autophagosome clearance, leading to cardiomyocyte necrosis and heart failure. Antioxid Redox Signal. 2016;25:10–27.

26. Kaludercic N, Carpi A, Nagayama T, Sivakumaran V, Zhu G, Lai EW, et al. Monoamine oxidase B prompts mitochondrial and cardiac dysfunction in pressure overloaded hearts. Antioxid Redox Signal. 2014;20:267–80.

27. Xiao MQ, Zhong HQ, Xia L, Tao YZ, Yin HY. Pathophysiology of mitochondrial lipid oxidation: role of 4-hydroxynonenal (4-HNE) and other bioactive lipids in mitochondria. Free Radic Bio Med. 2017;111:316–27.

28. Sparagna GC, Chicco AJ, Murphy RC, Bristow MR, Johnson CA, Rees ML, et al. Loss of cardiac tetralinoleoyl cardiolipin in human and experimental heart failure. J lipid Res. 2007;48:1559–70.

29. Zhao Y, Miriyala S, Miao L, Mitov M, Schnell D, Dhar SK, et al. Redox proteomic identification of HNE-bound mitochondrial proteins in cardiac tissues reveals a systemic effect on energy metabolism after doxorubicin treatment. Free Radic Bio Med. 2014;72:55–65.

30. Paillard M, Tubbs E, Thiebaut PA, Gomez L, Fauconnier J, Teixeira G, et al. Depressing mitochondria-reticulum interactions protects cardiomyocytes from lethal hypoxia-reoxygenation injury. Circulation. 2013;128:1555–65.

31. Dodson M, Wani WY, Redmann M, Benavides GA, Johnson MS, Ouyang X, et al. Regulation of autophagy, mitochondrial dynamics, and cellular bioenergetics by 4-hydroxynonenal in primary neurons. Autophagy. 2017;13:1828–40.

32. Dong Z, Shanmughapriya S, Tomar D, Siddiqui N, Lynch S, Nemani N, et al. Mitochondrial Ca(2+) Uniporter Is a Mitochondrial Luminal Redox Sensor that Augments MCU Channel Activity. Mol Cell. 2017;65:1014–28 e7.

33. Holmstrom KM, Pan X, Liu JC, Menazza S, Liu J, Nguyen TT, et al. Assessment of cardiac function in mice lacking the mitochondrial calcium uniporter. J Mol Cell Cardiol. 2015;85:178–82.

34. Pan X, Liu J, Nguyen T, Liu C, Sun J, Teng Y, et al. The physiological role of mitochondrial calcium revealed by mice lacking the mitochondrial calcium uniporter. Nat Cell Biol. 2013;15:1464–72.

35. Luongo TS, Lambert JP, Yuan A, Zhang X, Gross P, Song J, et al. The Mitochondrial Calcium Uniporter Matches Energetic Supply with Cardiac Workload during Stress and Modulates Permeability Transition. Cell Rep. 2015;12:23–34.

36. Yu Z, Chen R, Li M, Yu Y, Liang Y, Han F, et al. Mitochondrial calcium uniporter inhibition provides cardioprotection in pressure overload-induced heart failure through autophagy enhancement. Int J Cardiol. 2018;271:161–8.